

This work was written as part of one of the author's official duties as an Employee of the United States Government and is therefore a work of the United States Government. In accordance with 17 U.S.C. 105, no copyright protection is available for such works under U.S. Law.

Public Domain Mark 1.0

<https://creativecommons.org/publicdomain/mark/1.0/>

Access to this work was provided by the University of Maryland, Baltimore County (UMBC) ScholarWorks@UMBC digital repository on the Maryland Shared Open Access (MD-SOAR) platform.

Please provide feedback

Please support the ScholarWorks@UMBC repository by emailing scholarworks-group@umbc.edu and telling us what having access to this work means to you and why it's important to you. Thank you.

PROCEEDINGS OF SPIE

SPIDigitalLibrary.org/conference-proceedings-of-spie

Surface polarized reflectance analysis for aerosol remote sensing

Sergey Korkin, Alexei Lyapustin

Sergey Korkin, Alexei Lyapustin, "Surface polarized reflectance analysis for aerosol remote sensing," Proc. SPIE 11152, Remote Sensing of Clouds and the Atmosphere XXIV, 111520I (9 October 2019); doi: 10.1117/12.2531426

SPIE.

Event: SPIE Remote Sensing, 2019, Strasbourg, France

Surface polarized reflectance analysis for aerosol remote sensing

Sergey Korkin^{*a,b}, Alexei Lyapustin^b

^aUSRA GESTAR, 7178 Columbia Gateway Drive, Columbia, MD, USA 21046; ^bNASA GSFC, 8800 Greenbelt Rd., Greenbelt, MD, USA 20771

ABSTRACT

We study the Earth surface polarized reflectance using data collected by a space-based lidar. Accurate modelling of the surface reflectance supports retrieval algorithm development for the current and future Earth Science missions. Strong polarization of the laser light from Cloud-Aerosol Transport System (CATS) instrument, operated in 2015-2017, and nighttime measurements yield higher signal-to-noise ratio for polarization compared to the previous analysis of reflected, initially unpolarized, solar light.

Keywords: Earth surface polarized reflectance, space lidar, CATS.

1. INTRODUCTION

Knowledge of the ground surface reflectance, both for intensity and polarization, is important for studies of vegetation, soil, and atmosphere-surface interaction in general. In this paper, we further study how the ground surface reflects the polarized visible and near infrared light emitted by the Cloud-Aerosol Transport System (CATS)^{1,2}. CATS is a lidar Earth remote sensing instrument operated onboard the International Space Station (ISS) from February 2015 to October 2018. The CATS website³ is the source of the most up-to-date information about the system, products, and references.

To support the analysis of data from available (e.g., POLDER) and future (e.g. PACE, 3MI) missions, our research focuses on two questions:

1. Does the surface reflect polarization identically regardless of wavelength of the incident light?
2. Does the surface polarized reflectance obey the well-known Fresnel formulae for reflection of light by a flat facet⁴?

Research conducted from the 1990's to the early 2000's indicated that the above assumptions were true⁵⁻¹⁰. However, present day accuracy and reliability of the polarization-sensitive radiometers (polarimeters) have increased. Newer data has shown discrepancies between recent polarimetric measurements and previous studies and models. Listed below are some examples of observed discrepancy between recent measurements and the previous existing models, along with the solution attempted to resolve them:

- Shadow (e.g., from canopy) was added to correct the Fresnel reflection law^{11,12};
- The Fresnel reflection describes only mirror, also known as specular or glint, reflection. Recently, an addition term, responsible for scattering of light inside a leaf, was added¹², unfortunately at the expense of increase of the number of model parameters and the overall complexity of the model;
- The increase of the surface brightness observed with the Sun behind the observer, known in case of intensity as the Hot Spot¹³, was detected for polarization¹⁴. However, the existing models for polarized reflectance do not describe the Hot Spot¹⁵;
- Finally, spectral dependence of the surface polarized reflectance is assumed in the Airborne Multianagle SpectroPolarimetric Imager (AirMSPI) data processing algorithm^{16,17}.

Thus, the problem of observation and modelling of the surface polarized reflectance requires revisiting.

Previous satellite (POLarization and Directionality of the Earth Reflectance, POLDER⁵) and high-altitude airborne polarimeters (the NASA's Polarimeter Definition Experiment, PODEX) observed the Earth during daytime, when the atmospheric scattered solar light, with up to 10% degree of linear polarization^{18,19}, behaved as an unideal background. In situ measurements in laboratories or in the field are conducted from ~ 0.5-2 m from a target²⁰⁻²², providing much higher spatial resolution (each leaf is seen separately and often unshaded) than a satellite at ~ 400-600+ kilometers orbit. The

[*skorkin@usra.edu](mailto:skorkin@usra.edu)

surface reflectance is determined using different mathematical models for close versus distant observations. Low-altitude aircraft measurements suffer from atmospheric turbulence that causes aircraft altitude fluctuations and image distortion¹⁴. Regardless, low altitude aircraft images still possess higher resolution compared to satellites. These are a few examples of passive remote sensing utilizing a strong but unpolarized source of radiation – the Sun.

Unlike the Sun, the laser light is highly polarized. This increases the signal-to-noise ratio for the polarized studies, hence their accuracy, whereas night laser measurements avoid disturbing solar light scattered in the atmosphere. In laboratories, scientists routinely conduct laser studies of polarized reflectance for different patterns from a close distance. A space laser system has a very real potential for accurate characterization of the ground surface polarized reflectance on a global scale, however only at the backscattering direction (simulation of the hot spot cannot be checked). The same idea was used to calibrate the CALIPSO/CALIOP instrument using ground targets^{23,24}, and to retrieve the wind speed over the ocean^{25,26}. As far as we know, this is the first paper that investigates the possibility of analysis of the surface spectral polarized reflectance using space lidar.

2. THEORETICAL BACKGROUND

The lidar equation express the power, P , received by a lidar, from range (distance) r , as a function of lidar parameters and optical properties of atmosphere²⁷

$$P = P_0 \frac{Ah}{8\pi r^2} \beta_\lambda(r) \exp(-2\tau_\lambda), \quad (1)$$

where P_0 is the initial power, A is the receiver area, h is the laser pulse length, τ_λ is unitless optical depth between the receiver and the point r (one way). The backscattering coefficient, $\beta(r)$ [$\text{km}^{-1}\text{sr}^{-1}$], indicates how much scattering occurs at the point r . Both $\beta(r)$ and τ are, in general, unknown. Thus, the measured atmospheric parameter is the attenuated backscattering coefficient

$$\alpha_\lambda(r) = \beta_\lambda(r) \exp(-2\tau_\lambda). \quad (2)$$

Optical properties of the media, $\beta(r)$ and τ , depend on the wavelength, λ , and on the scattering substance (aerosol particles, clouds of water droplets, ice crystals, etc.). Surface is characterized by surface backscattering coefficient (also called surface return or echo signal), for which we will use the same notation, α .

Eq.(1) express the full received power, which is a sum of two components: parallel, \parallel , and perpendicular, \perp , with respect to plane of polarization of the outgoing laser beam (reference plane). Lidar atmospheric remote sensing often neglects the dependence of optical path, τ , on polarization²⁷. Thus, one deals with two independent equations, one per each of the components, and the total power

$$P_{\lambda}^{\parallel, \perp} = P_0 \frac{Ah}{8\pi r^2} \alpha_{\lambda}^{\parallel, \perp}(r); \quad P_{\lambda} = P_{\lambda}^{\parallel} + P_{\lambda}^{\perp}. \quad (3)$$

In general, the polarized light is described by a 4-component Stokes vector (T is the transpose operation)

$$\vec{S} = [I \quad Q \quad U \quad V]^T = [I_{\parallel} + I_{\perp} \quad I_{\parallel} - I_{\perp} \quad U \quad V]^T. \quad (4)$$

A diagonal scattering matrix²⁸

$$\vec{P} = \text{diag}[a_1 \quad a_2 \quad a_3 \quad a_4], \quad (5)$$

describes exact backscattering of laser light, initially 100% polarized in the parallel plane as:

$$\vec{P}\vec{S}_0 = \vec{P}[1 \quad 1 \quad 0 \quad 0]^T = [a_1 \quad a_2 \quad 0 \quad 0]^T; \quad I_{\parallel} = (a_1 + a_2)/2; \quad I_{\perp} = (a_1 - a_2)/2. \quad (6)$$

It follows from Eq.(6) that laser light does not get perpendicular component if backscattered by spherical particles or molecules of air (Rayleigh scattering) due to the equality: $a_1 = a_2$.

The Fresnel reflection matrix is widely used to simulate light reflection from surface, in particular, from waved ocean^{29,30}

$$\vec{F} = \begin{bmatrix} f_+ & f_- & 0 & 0 \\ f_- & f_+ & 0 & 0 \\ 0 & 0 & f_0 & 0 \\ 0 & 0 & 0 & f_0 \end{bmatrix}, \quad (7)$$

where « \leftrightarrow » denotes the square matrix whose elements are

$$\begin{aligned} f_{\pm} &= 0.5(f_{\parallel}^2 \pm f_{\perp}^2); \\ f_0 &= f_{\parallel}f_{\perp} \end{aligned} \quad f_{\parallel} = \frac{n^2 \cos(\theta_i) - \sqrt{n^2 - \sin^2(\theta_i)}}{n^2 \cos(\theta_i) + \sqrt{n^2 - \sin^2(\theta_i)}}, \quad f_{\perp} = \frac{\cos(\theta_i) - \sqrt{n^2 - \sin^2(\theta_i)}}{\cos(\theta_i) + \sqrt{n^2 - \sin^2(\theta_i)}}, \quad (8)$$

n is the refractive index (assumed real), and θ_i is the incidence angle. For exact backscattering, $\theta_i = 0^\circ$, the Fresnel reflection matrix becomes a diagonal one, surface roughness gives no shadow, rotation of the frame of reference does not occur. This results in the following form of the surface reflection matrix

$$\vec{p} = D(u) \text{diag}[\rho \quad \rho \quad -\rho \quad -\rho]; \quad \rho = \left(\frac{n-1}{n+1} \right)^2. \quad (9)$$

In Eq.(9), $D(u)$ defines the probability distribution of slopes. In case of ocean waves, it depends only on the wind speed, u ³⁰. Eq.(9) is the basis for all polarized surface reflectance models, discussed in the Introduction. It indicates that if the surface indeed reflects the light according to the Fresnel law then:

- if the surface is illuminated with a polarized light with no perpendicular component, the latter should not arise after the surface backscattering (reflection) – see Eq.(6);
- spectral dependence of the reflected signal is identical to spectral dependence of ρ in Eq.(9). For water, the real part of refractive index at 0.53 and 1.0 microns is 1.334 and 1.327, respectively³¹, which corresponds to 0.02048 and 0.01975 in ρ . This reduction of 3.6% suggests that the polarized reflectance from water should be smaller in the NIR. For Si, second most common element in the Earth crust, the corresponding values are $n(0.532; 1.064) = 4.137; 3.555$; $\rho(0.532; 1.064) = 0.3729; 0.3146$ (15% reduction in the NIR)³². Noteworthy, the polarized reflectance models currently assume $n=1.5$ with no spectral dependence.

In what follows, we check the both bullets using observation obtained from Cloud-Aerosol Transport System (CATS) space lidar.

3. METHODOLOGY

3.1 Basic information about CATS system

CATS is a NASA GSFC developed space lidar operated onboard the ISS at ~400km orbit, from February 10, 2015 to October 29, 2017. Several publications describe the goal and technical details of the mission^{1,2}, calibration³³, and data processing³⁴. The CATS website³ provides ATBDs and Release Notes, L1B and L2O (operational) data in hdf5 format, and examples of images.

The CATS system is similar to the Cloud-Aerosol Lidar with Orthogonal Polarization (CALIOP) lidar onboard the A-Train CALIPSO satellite²³. It provides vertical profiles of cloud and aerosol backscattering properties at 532nm and 1064nm bands with 60 m vertical resolution. The system operates in 3 different science modes depending on the number of laser beams involved. We are interested in mode 7.1, where 7 means “Science Mode”, which is a two-beam mode. However, unlike CALIPSO, the cross-polarized components are measured in both bands, while CALIOP/CALIPSO detects polarization at 532nm only. The $\pm 0.5^\circ$ off-nadir-deviation between the left and right beams (each is polarization sensitive at two bands) results in 7km distance between laser footprints, 14.38m in diameter; a narrow 110-microradians field of view (FoV) “*minimizes the impacts of solar background*”¹. The 7km distance between the footprints is close to 6km nadir resolution of the POLDER-type instruments^{5,35}. This provides an opportunity to estimate spatial variability of the surface polarized reflectance in addition to the spectral analysis. Figure 1, taken from the CATS paper³⁴, illustrates the measurement geometry. However, due to electrical failure, the 7.1 mode data is available only from February 10

through March 21, 2015 (40 days semi-continuous operation, with occasional interruptions for spacecraft docking at ISS), day and night.

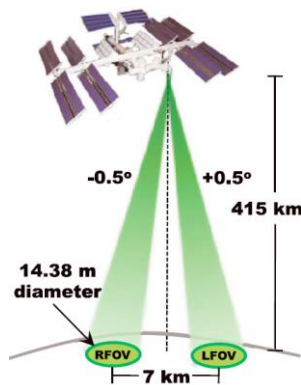


Figure 1. Geometry of observation. Image credit: Yorks et al, Geoph. Res. Lett. v.43, p.4633 (2016)³⁴.

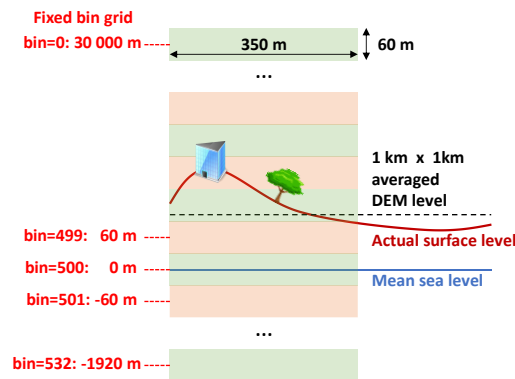


Figure 2. Vertical grid geometry. Multiple peaks within the same profile are possible due to landscape, natural and artificial elevations. The CATS data is given at fixed bin, 60m apart, defined with respect to mean sea level; 1km-averaged Digital Elevation Model (DEM) values are reported in CATS hdf-files.

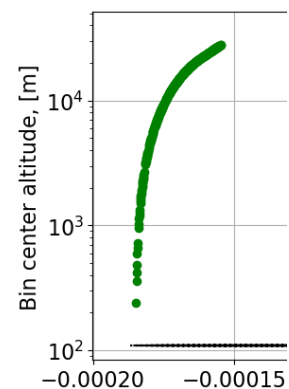


Figure 3. Negligibly small inaccuracy (negative backscattering on X-axis) occur after the Rayleigh correction. DEM value (black line) $\sim 100\text{m}$ is indicated.

Given the laser repetition rate of 5000Hz and the ISS velocity of about 7667m/s (according to Google), CATS receives signal every $7667/5000 = 1.5\text{m}$. To increase the signal-noise ratio, ~ 230 measurements are accumulated and averaged, yielding $\sim 350\text{m}$ along-the-track spatial resolution in L1B data.

Uncertainty in the calibration coefficient and signal noise contribute to measurement error. Yourks et al. GRL, (2016)³⁴ “demonstrate the ability to accurately detect optically thin atmospheric layers with 1064nm nighttime backscatter as low as $5 \cdot 10^{-5} \text{ km}^{-1}\text{sr}^{-1}$ ”. Due to significantly lower solar background signal (noise), the signal-to-noise ratio is higher for nocturnal measurements. For a cloudless atmosphere, the surface return is much stronger than that produced by a $\sim 5 \cdot 10^{-5} \text{ km}^{-1}\text{sr}^{-1}$ backscattering coefficient. Uncertainties in the CATS calibration coefficients³⁴ are estimated to be 5-10% at 532 and 10-15% at 1064 nm (for ice clouds during night time). Table 1³⁴ indicate the absolute values of the minimum detectable backscatter (MDB). For Mode 7.1, the MDB values for night is lower (hence, the SNR is higher) ~ 20 and ~ 40 times at 532nm 1064nm, respectively, compared to the day ones. This suggests that the night measurements are more accurate. However, given the small absolute values of the indicated MDBs, both day and night measurements can be used for surface characterization.

3.2 Data format and SDS used

The CATS data is available in 2 levels (L). Level 1B (L1B) data is calibrated and geolocated, meteorological data (e.g., temperature and pressure profile, surface wind velocity at 10m above the surface, etc.), computed atmospheric optical properties (molecular backscatter and 2-way transmittance, ozone mixing ratio), are provided. The profiles are interpolated to a fixed grid of heights (see Figure 2), and archived at the raw CATS resolutions: $\sim 350\text{m}$ horizontal, 60m vertical. This L1B data is used to derive the L2O data: profiles of aerosol and cloud properties (extinction, particle backscattering – not to be confused with total attenuated backscattering, Eq.(2)) and layer-integrated profiles (i.e. lidar ratio, optical depth). The L2O data comes at coarser resolution compared to L1B. The data is stored in tiles, each tile correspond to half orbit, about 45 minutes, day and night (twilight is captured and flagged in both). All the data is available from the CATS website³.

In this paper we use only L1B data, v.3.0. We are interested in the following Scientific Data Sets (SDS) in order of appearance in hdf5 file:

1. ancillary_data\surface reports the 1x1km averaged Digital Elevation Model (DEM) values and the International Geosphere-Biosphere Programme (IGBP)³⁶ land cover classification class (e.g., IGBP = 17: water bodies) for left (L), right (R) fields of view (FOV), and the nadir. Note, the DEM values are defined in meters.

2. `channel_1064\LFOV\Perpendicular_Attenuated_Backscatter1064_Left_FOV` contains an `nprof × nbins` array of 32-bit floating points, where the number of rows, `nprof`, is the number of profiles measured along the ISS track; `nprof=0` corresponds to acquisition start time. The number of profiles is recorded under `metadata_parameters\Number_Profiles` (e.g., `nprof=53268 → 53268·0.35km=18644km`). The number of columns, `nbins=533`, is the number of bins in the fixed grid of altitudes (Figure 2). This number is also available from `metadata_parameters\Number_Bins`; 0th bin is the TOA, ~30km above the mean sea level. The same information is available for band $\lambda=532\text{nm}$, right field of view (RFOV), and total attenuated backscatter

$$\alpha(\lambda, r) = \alpha_{\parallel}(\lambda, r) + \alpha_{\perp}(\lambda, r). \quad (10)$$

3. The `geolocation` SDS contains latitude (`lat`) and longitude (`lon`) for LFOV and RFOV.
4. `metadata_parameters\Bin_Altitude_Array` defines altitudes, in km, for middle of 60m-bins. It is a 1D array of size `nbins=533`. These altitudes, always starting from 30km [`ibin=0`] to -1.92km [`ibin=532`] are measured from to the mean sea level [`ibin=500`: altitude ≈ 0], see Figure 2 for clarification.
5. `metadata_parameters\Depol_Quality_Flag` one 16-bit integer per granule (one hdf5 file) notifies the users of granules with depolarization ratio of poor quality. We used only granules with 0 value indicating good quality of polarimetric data;
6. Finally, `profile_attributes\Day_Night_Flag` indicates if the observation happened during night (0), twilight (1), or daytime (2). In the examples below, we use only night measurements due to better signal-to-noise ratio.

Rayleigh contribution³⁷ was simulated numerically and subtracted from the total backscattering signal. As Figure 3 indicates, this cause an error, e.g. negative backscattering. However, the magnitude of this error is ~100-1000 times smaller compared to the level of the surface echo-signal. We currently ignore it.

4. RESULTS AND DISCUSSION

We start from analysis of 2 pixels (profiles) located in California (CA), on 16 Feb 2015: one in the wild area, another one in the urban area (Los Angeles - LA). In this case, the cloud-free zone was hand-picked. Figure 4 indicates the CATS track (4a) and cloud and aerosol loading along the track (4b). We took these two images from the CATS website³. Figure 4c and 4d show the location of the left and right fields of view for the 2 points in CA, and a landscape based on images from Google Earth.

Figure 5 shows the height profiles of the attenuated backscattering, Eq.(2), for the total (Fig. 5a) and perpendicular (Fig 5b) signal, for both spectral bands and both fields of view. A strong signal is observed close to the surface level (DEM value) for total and perpendicular backscattering. Magnitude of the signal at 1064nm is stronger, as expected, due to significantly smaller attenuation in atmospheric and higher surface reflectance. Two peculiarities are obvious:

- a) the perpendicular component of the backscattered signal is not predicted by the Fresnel-based model, Eq.(9), however it is detected;
- b) signal at the surface has two equal peaks at 2 neighboring bins, which may be caused by landscape (see Figure 2 and Figure 4c).

Table 1 reports numerical values for 2 strongest surface signals, bin altitudes and the DEM values.

Figure 6 shows similar results, but for the “urban” LA pixel. Again, a strong perpendicular component is measured in contrast to the prediction of the Fresnel-based polarized reflectance models. Table 2 reports numerical values for this case, but only for one bin with the strongest signal.

For general conclusions, many pixels must be analyzed. Out of all pixels along the track, Fig. 4a, we need to pick only those where land is clearly seen: no clouds and significant aerosol loading. To select the land pixels, we use the following criteria for both L & R FOVs:

- i) Using IGBP index from CATS hdf-files, we skip pixels marked as water, ice or snow;

- ii) We consider pixels that are brighter in 1064nm than in 532nm in terms of total backscattering signal;
- iii) Bin altitudes for the pixels selected after (i) and (ii) differ from the hdf DEM value by no more 500m.

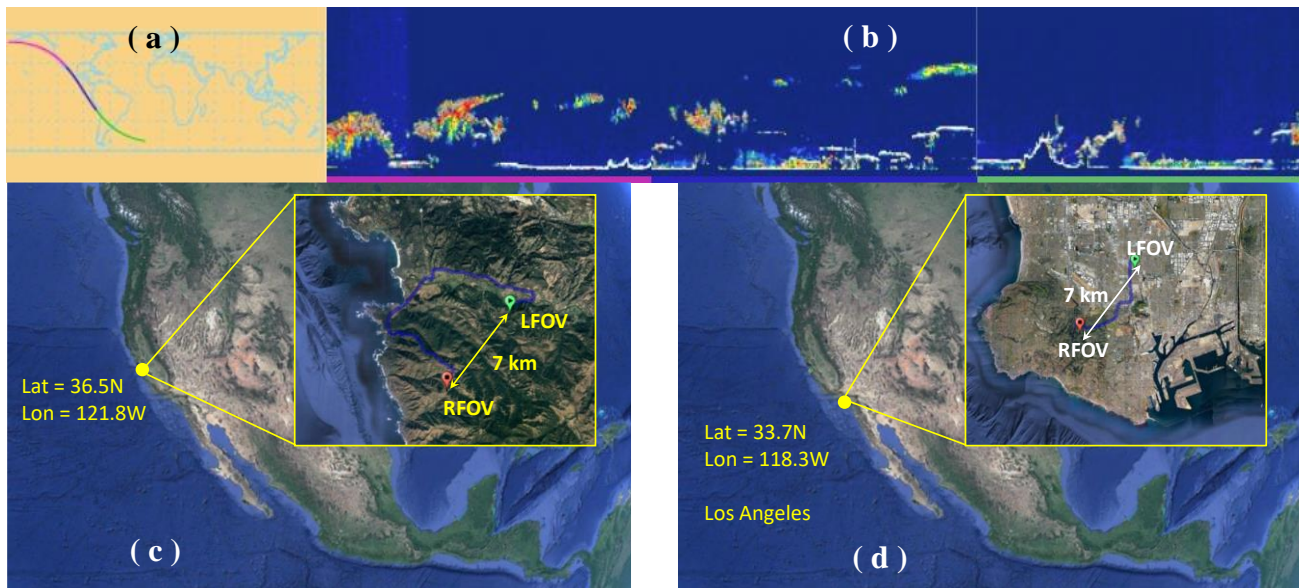


Figure 4. The CATS track (a) and cloud-aerosol loading (b) along the track, as shown on the CATS website³ and location of 2 cloud-free pixels in CA (wild area (c) and Los Angeles (d)) according to Google Earth. Tile name: CATS-ISS_L1B_N-M7.1-V3-00.2015-02-16T05-42-52T06-27-16UTC.hdf5 (note, N stands for night measurements).

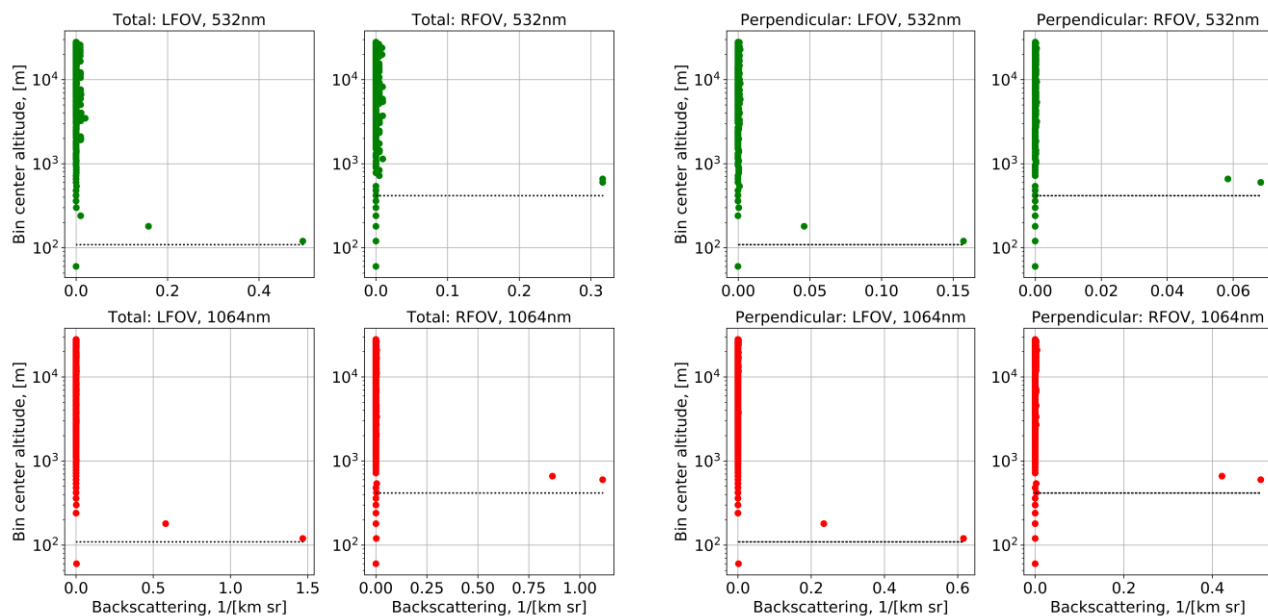


Figure 5a. Total attenuated backscattering for left and right footprints for the “wild” pixel in CA – see Fig.4c. Green and red correspond to bands 532nm and 1064nm, respectively. Horizontal dash line is the DEM level. See Table 1 below for numerical values.

Figure 5b. Same as Figure 5a, except for perpendicular backscattering component. As opposed to the Fresnel-based models, a strong perpendicular component exists in the backscattered signal.

To eliminate the effect of atmosphere, for the selected pixels we consider the ratio of the attenuated backscattering coefficients:

$$\alpha_{\perp}(\lambda,r)/\alpha_{\parallel}(\lambda,r)\approx\beta_{\perp}(\lambda,r)/\beta_{\parallel}(\lambda,r)=\beta_{\perp}(\lambda,r)/(\beta(\lambda,r)-\beta_{\perp}(\lambda,r))\, . \tag{11}$$

Since we select only data with Depol_Quality_Flag=0, we assume similar calibration error for both parallel and perpendicular components and that Eq.(11) holds true with sufficient accuracy. Figure 7 shows results for both sides and bands for the CA track, Fig.4, where we picked ~2500 pixels. Both top scatter plots are noticeably far from the 1:1 line, which indicates spectral dependence of the ratio for both left and right fields of view. Bottom row shows scatter plots for right vs left fields of view at given bands 532nm (bottom-left) and 1064 (bottom-right). For a sufficiently long track, the left-vs-right scatter plot should be symmetric with respect to 1:1 line, which is the case of band 532nm (bottom-left). However, at 1064nm, the distribution is not symmetric with respect to 1:1 line. Note, we used the same axis-limits for all four subplots.

Table 1. Numerical results for 2 strongest signals in Figure 5

Signal, [km ⁻¹ sr ⁻¹]	Total		Perpendicular	
	L	R	L	R
Side >				
532 nm >	0.497 & 0.158	0.316 & 0.316	0.157 & 0.046	0.068 & 0.058
1064 nm >	1.470 & 0.581	1.112 & 0.867	0.617 & 0.235	0.510 & 0.422
Bin altitude, m >	120 & 180	600 & 660	120 & 180	600 & 660
DEM value, m >	109	417	109	417

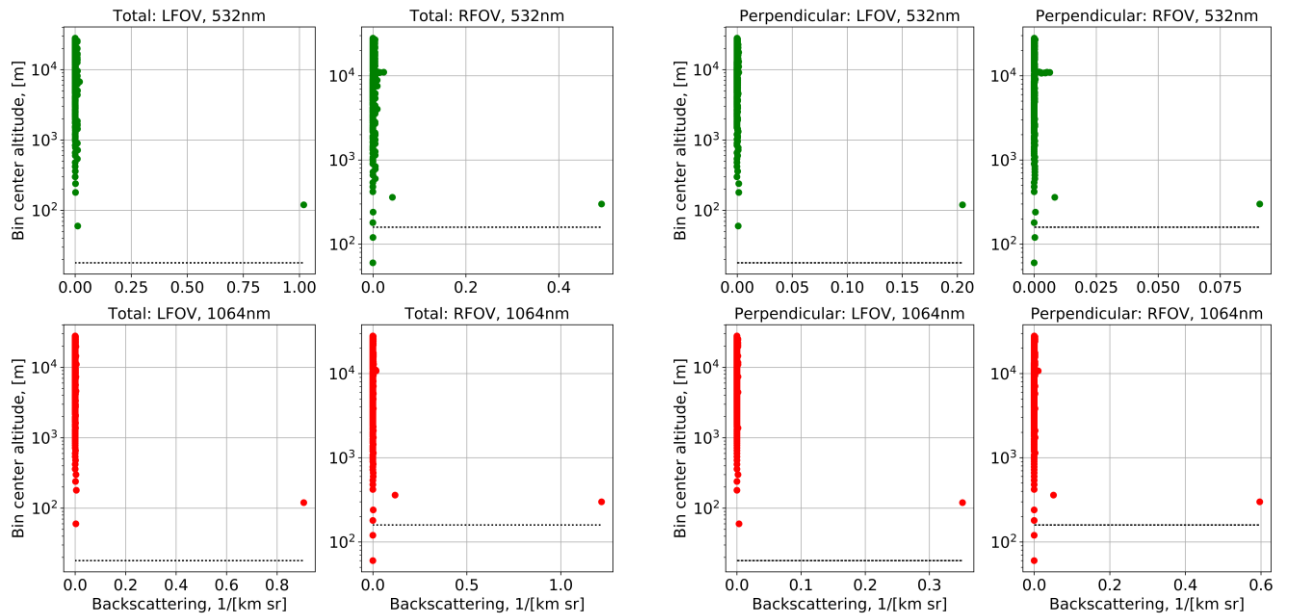


Figure 6a. As in Figure 5a, but for the urban pixel – Figure 4d; see Table 2 for numerical results.

Figure 6b. As in Fig.5b, except for urban pixel, Fig. 4d.

Table 2. Numerical results for the strongest signal shown in Figure 6.

Signal, [km ⁻¹ sr ⁻¹]	Total		Perpendicular	
	L	R	L	R
Side >				
532 nm >	1.021	0.493	0.205	0.091
1064 nm >	0.907	1.216	0.351	0.598
Bin altitude, m >	120	300	120	300
DEM value, m >	18	160	18	160

Figure 8 shows analysis like in Figure 7, but for African track and ~6500 points selected using the same criteria. In general, the shape of the scatter plots is similar: both subplots in the top row indicate spectral dependence for left and right fields of view. Bottom left (right vs left signal for 532 nm) is, as we expect, is closer to 1:1 line. However, the 1064 nm scatter plot for left vs right sides (bottom right) is again noticeably non-symmetric with respect to 1:1 line.

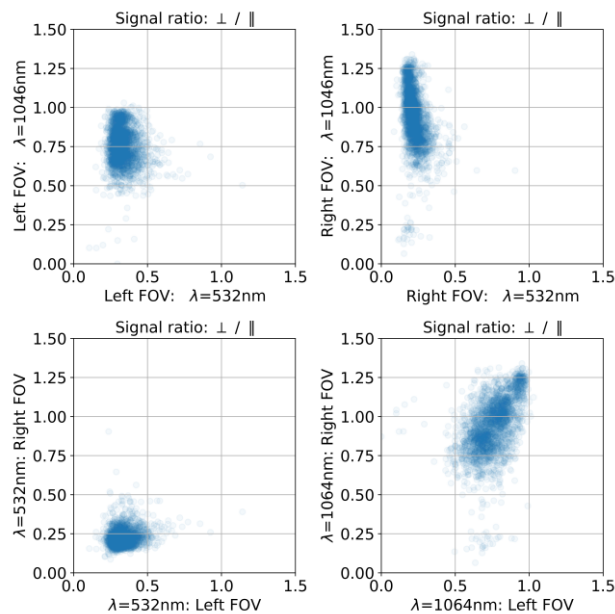


Figure 7. Scatter plots for ratio of parallel to perpendicular attenuated backscattering signal. Top row: 1064nm vs 532nm for left, and right fields of view, respectively. Bottom row: RFOV vs LFOV for 532nm (bottom-left) and 1064nm (bottom-right)

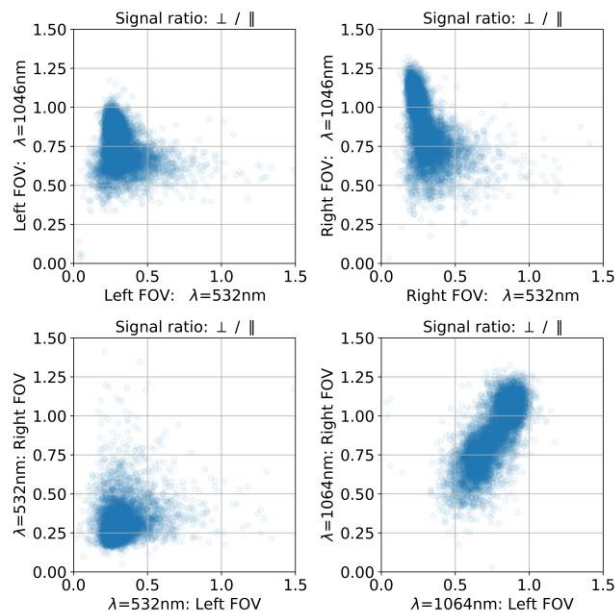
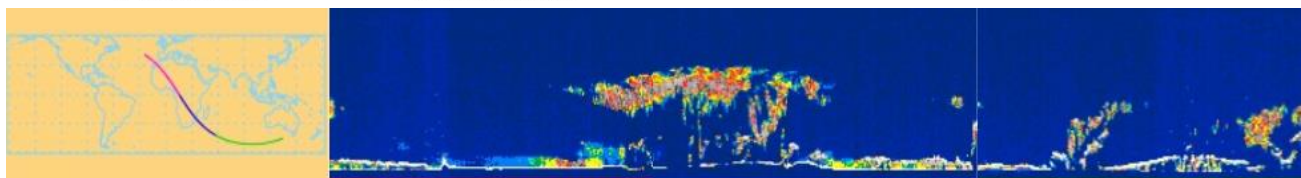


Figure 8. Same as in Figure 7, but for the African track on 23 Feb 2015 (~6500 pixels). We took images of the track and the backscattering profile along the track from the CATS website³ – both shown below the scatterplots. Corresponding granule hdf file name: CATS-ISS_L1B_N-M7.1-V3-00.2015-02-23T19-51-51T20-35-58UTC.hdf5



5. CONCLUSION

We have analyzed the land polarized backscattering in 2 bands, 532nm and 1064nm, using CATS attenuated backscattering. Contrary to the Fresnel-based surface polarized reflectance models, we see a strong perpendicular component in the backscattering of the laser light in both bands. Also contrary to the Fresnel models, the ratio of the parallel-to-perpendicular components is band-dependent. Contrary to our expectation, there is a noticeable difference in the ratio of the cross-polarized components for left and right fields of view at 1064nm along two tracks: one over the American east coast, and one over Africa.

Our reported results are preliminary and aim to proof the concept of the surface spectral polarized reflectance analysis using space lidar. We plan to continue our research by improving our clean atmosphere/surface detection algorithm and including day measurements in addition to the nocturnal ones for broader statistics. For the day measurements, we plan to use the total atmosphere optical thickness available from passive remote sensing systems in order to analyze the absolute value of the surface echo signal for cross-polarized components instead of their ratio. For that, the ISS position must be collocated with e.g. the A-Train instruments. Similar analysis can be conducted during nighttime at the vicinity of the AERONET sites where nocturnal measurements are available. We may need to “recalibrate” the surface reflectance measurements based on the assumption of average equality of signal coming from either side along the CATS track. Finally, we plan to analyze the polarized reflectance from ocean, for which the Fresnel surface polarized reflectance model should provide good results, possibly after averaging from 350m to a coarse spatial resolution.

ACKNOWLEDGEMENTS

The work of S.Korkin is funded by USRA Research and Development (R&D) program. We took Figure 1 from the CATS paper³⁴ and images of 2 CATS tracks and 2 backscattering profiles in Figs. 4 and 8 from the CATS website³. S. Korkin is thankful to P. Selmer for help with the CATS hdf5-files and to A. Sayer for pointing to related papers^{25,26}.

REFERENCES

- [1] McGill, M., Welton, E., Yorks, J., and Scott, S., “CATS: a new Earth science capability”, *The Earth Observer* 24(3), 4-8 (2012).
- [2] McGill, M., Yorks, J., Scott, V., Kupchock, A., and Selmer, P., “The Cloud-Aerosol Transport System (CATS): a technology demonstration on the International Space Station”, *Proc. SPIE* 9612, *Lidar Remote Sensing for Environmental Monitoring XV*, 96120A (2015), DOI: 0.1117/12.2190841.
- [3] <https://cats.gsfc.nasa.gov/> (accessed: 21 July 2019).
- [4] Born, M., and Wolf, E., [Principles of optics], Pergamon Press, New York, 2nd edition (1964).
- [5] Deschamps, P., Breon, F., Leroy, M., Podaire, A., Bricaud, A., Buriez, J., and Seze, G., “The POLDER mission: instrument characteristics and scientific objectives”, *IEEE Trans. Geosci. Rem. Sens.* 32 (3), 598-615 (1994).
- [6] Breon, F.-M., Tanre, D., Lecomte, P., and Herman, M., “Polarized reflectance of bare soils and vegetation: measurements and models”, *IEEE Trans. Geos. Rem Sens.* 33 (2), 487-499 (1995).
- [7] Nadal, F., and Breon, F.-M., “Parametrization of surface polarized reflectance derived from POLDER spaceborne measurements”, *IEEE Trans. Geos. Rem Sens.* 37(3), 1709-1718 (1999).
- [8] Maignan, F., Breon, F.-M., Fedele, E., and Bouvier, M., “Polarized reflectances of natural surfaces: spaceborne measurements and analytical modeling”, *Rem. Sens. Env.*, 113, 2642-2650 (2009).
- [9] Tanre, D., Breon, F.-M., Deuze, J., Dubovik, O., Ducos, F., Francois, P., Goloub, P., Herman, M., Lifermann, A., and Waquet, F., “Remote sensing of aerosols by using polarized, directional and spectral measurements within the A-Train: the PARASOL mission”, *Atmos. Meas. Tech.* 4, 1383-1395 (2011).
- [10] Yang B., Zhao, H., and Chen, W., “Semi-empirical models for polarized reflectance of land surfaces: intercomparison using space-borne POLDER measurements”, *J. Quant. Spectrosc. Rad. Trans.* 202, 13-20 (2017).
- [11] Cairns, B., Russell, E., and Travis, L., “The Research Scanning Polarimeter: Calibration and ground-based measurements”, *Proc. SPIE*, 3754, 186-197 (1999).
- [12] Litvinov, P., Hasekamp, O., Dubovik, O., and Cairns, B., “Model for land surface reflectance treatment: Physical derivation, application for bare soil and evaluation on airborne and satellite measurements”, *Rem. Sens. Env.* 115, 781-792 (2012).

- [13] Maignan, F., Breon, F.-M., and Lacaze, R., “Bidirectional reflectance of Earth targets: Evaluation of analytical models using a large set of spaceborne measurements with emphasis on the Hot Spot”, *Rem. Sens. Env.* 90 (2), 210-220 (2004).
- [14] Diner, D., Xu, F., Garay, M., Martonchik, J., Rheingans, B., Geier, S., Davis, A., Hancock, B., Jovanovic, J., Bull, M., Capraro, K., Chipman, R., and McClain, S., “The Airborne Multiangle SpectroPolarimetric Imager (AirMSPI): a new tool for aerosols and cloud remote sensing”, *Atmos. Meas. Tech.* 6, 2007-2025 (2013).
- [15] Sun, Z., Peng Z., Wu, D., and Lv, W., “Photopolarimetric properties of leaf and vegetation covers over a wide range of measurement directions”, *J. Quant. Spectrosc. Radiat. Transfer* 206, 273-285 (2018).
- [16] Xu, F., Dubovik, O., Zhai, P.-W., Diner, D., Kalashnikova, O., Seidel, F., Litvinov, P., Bovchaliuk, A., Garay, M., van Harten, G., and Davis, A., “Joint retrieval of aerosol and water-leaving radiance from multispectral, multiangular and polarimetric measurements over ocean”, *Atmos. Meas. Tech.* 9, 2877-2907 (2016).
- [17] Xu, F., van Harten, G., Diner, D., Kalashnikova, O., Seidel, F., Bruegge, C., and Dubovik, O., “Coupled retrieval of aerosol properties and land surface reflection using the Airborne Multiangle SpectroPolarimetric Imager”, *J. Geophys. Res. Atmos.* 122, 7004-7026 (2017).
- [18] Adams, C., and Kattawar, G., “Solutions of the equations of radiative transfer by an invariant imbedding approach”, *J. Quant. Spectrosc. Radiat. Transfer* 10 (5), 341-356 (1970).
- [19] Mishchenko, M., Lacis, A., and Travis, L., “Errors induced by the neglect of polarization in radiance calculations for Rayleigh-scattering atmospheres”, *J. Quant. Spectrosc. Radiat. Transfer* 51(3), 491-510 (1994).
- [20] Sun, Z., Wu, D., Lv, Y., and Zhao, Y., “Polarized reflectance factors of vegetation covers from laboratory and field: A comparison with modeled results”, *J. Geophys. Res. Atmos.* 122, 1042-1065 (2017).
- [21] Peltoniemi, J., Hakala, T., Suomalainen, J., and Puttonen, E., “Polarised bidirectional factor measurements from soil, stones and snow”, *J. Quant. Spectrosc. Radiat. Transfer* 110, 1940-1953 (2009).
- [22] Suomalainen, J., Hakala, T., Suomalainen, J., Puttonen, E., and Peltoniemi, J., “Polarised bidirectional factor measurements from vegetated land surfaces”, *J. Quant. Spectrosc. Radiat. Transfer* 110, 1940-1953 (2009).
- [23] Winker, D.M., and coauthors, “Overview of the CALIPSO Mission and CALIOP Data Processing Algorithms,” *J. Atmos. Oceanic Technol.*, 26, 2310–2323 (2009).
- [24] Powell, K.A., and coauthors, “CALIPSO Lidar Calibration Algorithms. Part I: Nighttime 532-nm Parallel Channel and 532-nm Perpendicular Channel,” *J. Atmos. Oceanic Technol.* 26, 2015–2033 (2009).
- [25] Hu, Y., et al. “Sea surface wind speed estimation from space-based lidar measurements”, *Atmos. Chem. Phys.*, 8(13), 3593-3601, (2008).
- [26] Hu Y., and Nee, J., “High resolution sea surface wind speed from CALIOP measurements”, *Light, Energy and the Environment*, OSA Technical Digest (online), doi: <https://doi.org/10.1364/E2.2014.EW3A.2>.
- [27] Gimmestad, G., “Reexamination of depolarization in lidar measurements”, *Appl. Opt.* 47(21), 3795-3802 (2008).
- [28] Mishchenko, M.I., and Hovenier J.W., “Depolarization of light backscattered by randomly oriented nonspherical particles”, *Optics Lett.*, 20(12), 1356-1358 (1995).
- [29] Emde, C., Barlas, V., Cornet, C., Evans, F., Korkin, S., Ota, Y., C.-Labonnote, L., Lyapustin, A., Macke, A., Mayer, B., and Wendisch, M., “IPRT polarized radiative transfer model intercomparison project – Phase A”, *J. Quant. Spect. Rad. Trans.* 164, 8-36 (2015).
- [30] Nakajima, T., and Tanaka, M., “Effect of wind-generated waves on the transfer of solar radiation in the atmosphere–ocean system”, *J. Quant. Spect. Rad. Trans.* 29, 521-537 (1983).
- [31] Hale, G.M., and Querry, M.R., “Optical constants of water in the 200-nm to 200-μmwavelength region,” *Appl. Opt.* 12, 555–563 (1973).
- [32] <https://refractiveindex.info/> (accessed: 21 July 2019).
- [33] Pauly, R., Yorks, J., Hlavka, D., McGill, M., Amiridis, V., Palm, S., Rodier, S., Vaughan, M., Selmer, P., Kupchok, A., Baars, H., and Gialitaki, A., “Cloud Aerosol Transport System (CATS) 1064 nm calibration and validation”, *Atmos. Meas. Tech. Disc.* 172, 1-22 (2019).
- [34] Yorks, J., McGill, M., Palm, S., Hlavka, D., Selmer, P., Nowotnick, E., Vaughan, M., Rodier, S., and Hart, W., “An overview of the CATS level 1 processing algorithms and data products”, *Geophys. Res. Lett.* 43, 4632-4639 (2016).
- [35] Marbach, T., Phillips, P., Lacan, A., Schlüssel, P., “The Multi-Viewing, Multi-Channel, Multi-Polarisation Imager (3MI) of the EUMETSAT Polar System - Second Generation (EPS-SG) dedicated to aerosol characterization”, *Proc. SPIE*, 8889, 344-347 (2013).
- [36] <https://climatedataguide.ucar.edu/climate-data/ceres-igbp-land-classification> (accessed: 21 July 2019)
- [37] Bodhaine, B., Wood, N., Dutton, E., and Slusser, J., “On Rayleigh optical depth calculations”, *J. Atm. Ocean Technol.* 16, 1854-1861 (1999).